



# Investigating the Multiscale Micromechanical Properties of Sembar Shale in the Southern Indus Basin, Pakistan through Nanoindentation

**Darya Khan Bhutto\***

*Institute of Petroleum and Natural Gas Engineering, Mehran University of Engineering and Technology, Jamshoro, Pakistan;  
Department of Petroleum and Gas Engineering, Dawood University of Engineering and Technology, Karachi, Pakistan*

\*Corresponding author

**Ubedullah Ansari**

*Institute of Petroleum and Natural Gas Engineering, Mehran University of Engineering and Technology, Jamshoro, Pakistan*

**Aftab Ahmed Mahesar**

*Institute of Petroleum and Natural Gas Engineering, Mehran University of Engineering and Technology, Jamshoro, Pakistan*

**Najeeb Anjum Soomro**

*Department of Petroleum and Gas Engineering, Dawood University of Engineering and Technology, Karachi, Pakistan*

## Abstract

The Sembar Shale in Pakistan is considered to possess large volumes of unconventional energy resources. To assess the reservoir micromechanical properties of Sembar shale is essential to ascertain the hardness and elastic modulus while injecting CO<sub>2</sub> and to perform hydraulic fracturing operations; however, no study has yet been conducted to enumerate such properties. Such parameters provide guidelines for proppant selection and may affect the designing and optimization strategies of drilling complex boreholes and fracturing treatments. Thus, to achieve this, the experiments were performed with the hierarchy of mineral identification via X-ray diffraction (XRD), microstructural description via scanning electron spectroscopy (SEM) studies, and elemental compositional analysis via energy dispersive spectroscopy (EDS) and the nanoindentation, atomic force microscopy (AFM). The mineral composition of shale was assessed via XRD and the shale composition was analysed concerning clay minerals, organic matter, and with other minor mineral contents. The analysis of Young's modulus variation is conducted by examining recorded indentation depth curves and modulus distributions. It is obvious from our results that there is a significant difference in the modulus of elasticity and hardness of selected samples. The hardness (indentation moduli, GPa) of shale sample B was significantly lower than shale sample A. This shows that the shale sample A relatively displayed elastic deformation and recovery after the loading and unloading sequence. It was further noticed that the micro-cracks were generated in shale sample A corresponding to indent penetration; conversely, the micro-cracks in shale sample B were not propagated for applied indentation loading. Such variations occurred in both samples due to the changes in grain orientations and compaction at the time of deposition. The smaller hardness and lower elastic modulus values observed from the shale sample B show an underestimation of rock strength, which in turn may affect the proppant selection and settlement as well as embedment during fracturing jobs. Thus, the study provides an understanding of decision-making and designing drilling operations and fracking treatments for shale gas oil reservoirs.

## Keywords

Micromechanical properties, Nanoindentation, AFM, Sembar shale, Southern Indus Basin

## 1. Introduction

Every year, there is a huge increase in the amount of energy consumed; thus, the only way to meet the growing energy demand is to develop the currently available unconventional resources [1, 2]. It appears that conventional energy resources are not sufficient to accomplish such huge demand. Pakistan also faces severe energy problems, there is a large gap between demand and supply of energy [3-5]. Surprisingly, the nation's sedimentary basins have enormous untapped resource potential [6-9]. Hence, unconventional energy resources are considered to be the better substitute to contribute

from organic-rich shale formations to fulfill the present-day demand. Even though, the industry is not yet effective, particularly in designing fracturing jobs for shale formation due to several complications. Because of their distinct geomorphological, petrophysical, elastic, and plastic behaviors as well as their depositional environments, unconventional reservoirs are typically characterised by poor porosity and extremely low permeability in nano-darcies [10]. Even less is known about the shale gas deposits in Pakistan's Lower Indus Basin's Sembar Shale Formation. Earlier studies on shales from Sembar formation have generally focused on the differences in geological aspects, seismic attributes, mineralogy, geochemistry, adsorption capacity to some extent, and porosity and permeability derived from log data [11, 12]. To the best of the authors' knowledge, no research has been done to date to shed light on the mechanical behavior of these shales. Understanding the micromechanical characteristics of the selected reservoir would be very beneficial for its effective development and utilization. Furthermore, the mechanical characteristics of shales are important for comprehending the fundamental factors that affect the design of hydraulic fracturing treatments for better recovery. In more recent times, the storage of CO<sub>2</sub> and hydrogen has grown to be crucial to several initiatives [13, 14]. Usually, the CO<sub>2</sub> and H<sub>2</sub> are stored in depleted reservoirs which are overlain by shale formations layers [14]. Thus, the induced stress due to CO<sub>2</sub> injection may mechanically damage top seals. In addition, it may trigger the seismic activity at storage sites which in turn induce fracturing of the formation. Therefore, assessing the mechanical behaviour of shale formation seal integrity is essential in preventing caprock fracturing.

Subsequently, the economic production from shale gas reservoirs can only be achieved by drilling horizontal wells and performing fracturing jobs to create fractures that widen the flow paths [15]. Hence, the induced fractures via hydraulic fracturing and propagated cracks depend on the stress and strain rate [16]. Since large-size samples are needed for traditional rock mechanical property measurement techniques like triaxial testing to determine the rock's mechanical characteristics on a macroscopic scale, Such procedures did not yield mechanical properties of shales at the nanoscale, and neither provide information on individual mineral constituents [17]. Tri-axial and uniaxial tests are usually performed on outcrop samples obtained from exposed shale formations, and the measurements are made on a small number of reservoir samples of shales [18, 19]. This is because the lack of cores from the reservoir and is hard to make take cylindrical size samples due to friable nature of shale formations. So, the application of nanoindentation is one of the most effective techniques to characterize the micromechanical properties of shales [20-22].

Generally, shale rocks are considered to be composed of complex minerals, the rock from the same formation may behave differently. [23] Though, it is crucial to understand the mechanical behaviors of such formations explicitly; which can only be achieved by indentation experiments at microscale [24]. Subsequently, there exist many other complications to shale formation such as borehole wall instability, shrinking of wellbore walls due to clay swelling, borehole collapsing, and wellbore tensile damage are the key issues that need to be assessed [25]. In order to drill a well, drilling fluids like water-based muds must be injected. This creates hydration and swelling issues in shale formations, which lowers the strength of the rock and can lead to borehole collapse or diameter shrinkage [26]. Pakistan's upper Indus basin formations have encountered such issues of wellbore stability during drilling operations (e.g. Laljee, et al., 2021) [27]. Thus, mechanical properties assessment is essential in designing drilling operations.

Numerous experimental and theoretical studies have been conducted to understand how rock mechanical properties are affected [1, 4, 28, 29]. Chen et al. (2007) analyzed the shale formation hardness and elastic modulus via micro-mechanical test and suggested a model for estimation of mechanical properties of rocks at microscale [30]. Although there is a great deal of micromechanical data on shale formations in other parts of the world, no study to far has provided data on the features of Sembar shale deposits at the nanoscale [19, 31-34]. Large differences are reported in sediment sources, sediment deposition, and diagenesis among different shales as a result the geo-mechanical characteristics may vary. Shale rock's geomechanical properties assessment via AFM and nanoindentation at nano-to-micro-scale is a new addition to traditional geo-mechanical investigations. Therefore, the accurate analysis, determination, and comparison of the variations in micro-mechanical characteristics was the goal of this research. The study involved in this paper performed a comprehensive analysis of the rock strength properties of the samples from two different locations of outcrop via surface topography assessments via atomic force microscopy, mineralogy via X-ray diffraction analysis, and microstructural description.

### 1.1 Geology of study area

The samples were obtained from the southeastern margin of the Kirthar Fold Belt (Pab Mountain Range), the Winder Valley area, and the Winder-Kanrach Sections as depicted in Figure 1. The generalized stratigraphic column of the southern Indus Basin is shown in Figure 2. The Fieldwork was done in the main stratigraphic sections of Sembar Pass near Winder Valley areas and along the roadside of the Winder-Kanrach, in the Lower Indus Basin, Baluchistan, Pakistan. The Sembar Formation name was first introduced by Williams in years (1959) and is exposed in the outcrop successions in the Lower Indus Basin, Pakistan. Sembar formation is around two kilometres in the Southeast direction of the Sembar Pass in the Marri-Bugti mountains of the Sulaiman fold belt Range with North Latitude 29° 56' 05" and East Longitude, 68° 32' 45". The formation lies in the early cretaceous strata of the regional geological sequence stratigraphy. Further, the Hunting Survey Corporation (1961) included the Sembar formation as a basal unit of the Parh formation series. Sembar shale comprises the black, greenish, and silty with interbedded siltstones and weathered limestone and iron ores are noticed as a nodular. [35] Moreover, a tina alluvium cover was observed in patches across the outcrop. The Sembar

formation at the studied location observed was dark brown comprised of volcanic rock masses along with ophiolites near the Bela ophiolite complex. The thick-bedded dark-colored Chiltan limestone formation is also in contact with the Cretaceous Sembar shale Formation [36]. The Chiltan formation exists in Southern Indus Basin and is extended to depths of 4500m with varying texture from fine-grained to oolitic and reefoid [37]. Several rocks are found to be present within sediments of cretaceous formation consisting of shale, limestone sandstone, and interbedded siltstones [38]. The Sembar Shale formation exposed near Winder city of Baluchistan exhibited very complex lithology of light grey to black color. These shales outcrops were slightly hard at the bottom of the Pab mountain range and around a few places it was very brittle as well as soft shale clayey sands. The Sembar shale is interbedded with thin limestone and sandstone nodules[39].

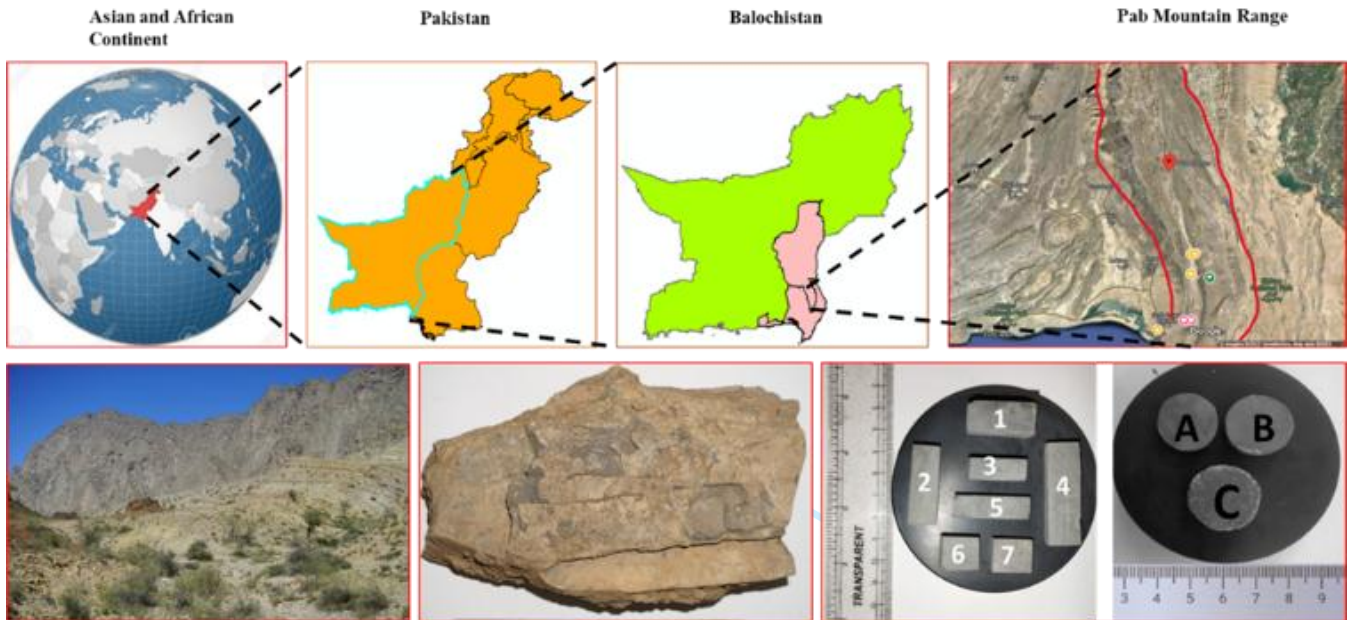


Fig. 1 Geological map of the study area displaying the field location, sampling sites, collected hand specimen, And prepared samples of the Sembar Shale in the Southern Indus Basin, Pakistan

AGE				DESCRIPTION	LITHOLOGY	
ERA	PERIOD	EPOCH	FORMATION			
MESOZOIC	CRETACEOUS	LATE	PAB	SANDSTONE, SHALE	[Pattern: horizontal lines]	
			MUGHAL KOT	LIMESTONE, SHALE WITH MINOR SANDSTONE	[Pattern: horizontal lines with dots]	
			PARH	LIMESTONE	[Pattern: horizontal lines with dots]	
		MIDDLE	GORU	UPPER	MARLY SHALE	[Pattern: horizontal lines with dots]
				LOWER	SANDY SHALE	[Pattern: horizontal lines with dots]
		EARLY	SEMBAR	OIL/GAS SHALE WITH MINOR SANDSTONE	[Pattern: horizontal lines with dots]	
	JURASSIC	LATE			[Pattern: horizontal lines with dots]	
		MIDDLE	CHILTAN	LIMESTONE	[Pattern: horizontal lines with dots]	
		EARLY	SHIRINAB	LIMESTONE, SHALE, SANDSTONE	[Pattern: horizontal lines with dots]	
	TRIASSIC	EARLY-LATE	WULGAI	SANDSTONE, SHALE	[Pattern: horizontal lines with dots]	
CAMBRIAN NOT ENCOUNTERED						

Fig. 2 Stratigraphic column showing the wide range of geological sequences of Indus Basin, Pakistan (Modified after Sohail et al., 2020) [40]

## 2. Materials and Methods

### 2.1 Materials

The study required fieldwork to gather samples and to carry out experimental work. Samples of various sizes were therefore gathered along the Khurkhera-Kanjraj Road, which runs close to the southeast of Winder City in Baluchistan, Pakistan (Table 1). These shales were analysed to describe the mineralogical, and microstructural characteristics, and to obtain the micromechanical parameters. A portion from each sample was obtained by cutting into parts to make a suitable sample for tests to be performed. The sample geo-mechanics and micro-texture at different scales of shale samples were analysed via high-resolution FE-SEM techniques. Thereafter, the micromechanical parameters were determined for shale samples from two locations, i.e., Figure 3(a & b).

**Table 1** Summary of the experiments performed, and number of samples analysed

Location	Stations	Sample ID	XRD	SEM	AFM	Vickers Micro Hardness	Nanoindentation
Khurkhera-Kanjraj Road, Baluchistan, Pakistan (Pab Mountain Range)	Near Winder city area, Baluchistan	22-SMB-02b	X	X	X	√	√
		22-SMB-03a	√	√	√	√	X
		22-SMB-04a	√	√	√	√	√
		22-SMB-04c	X	√	X	√	X

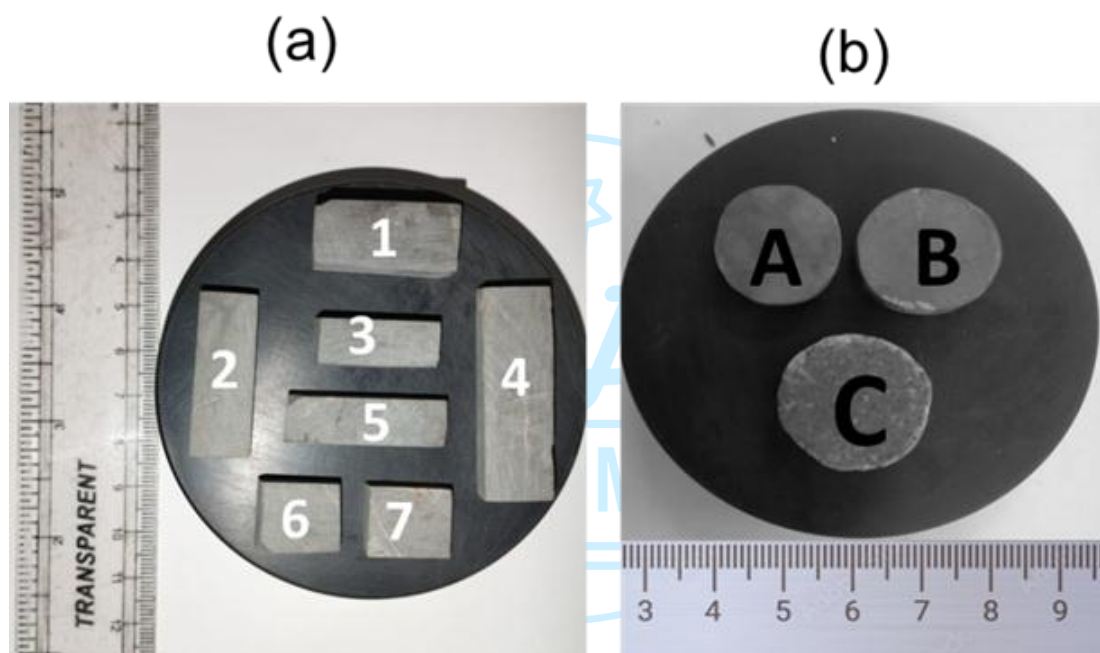


**Fig. 3** Two types of shale samples prepared for testing (a) cubical samples. (b) cylindrical samples

### 2.2 Sample Preparation

For the AFM, SEM, and nanoindentation tests, a parallel piece of sample was cut and cored from intact Shale samples. The sample surface needs to be perfectly smooth and mirror-like to yield accurate results. Therefore, the sample surfaces were grinded and polished on the end face grinder machine. The extent of sample smoothness reflection depends upon the sample surface shining. The more will be smoothness in the surface, the more reflective is surface. Sample surface smoothness was performed via mechanical polishing, grinding, and polishing using oil-based diamond suspension. Generally, it is recommended to use oil-based suspensions for surface smoothness to avoid hydration and any adverse reaction effects on Shale samples. In addition, it is suggested that the surface roughness should not exceed one-fifth of the typical depth of nanoindentation [19]. It is also recommended to avoid using water while polishing, grinding, or preparing samples since it reacts with shale and might change the physical characteristics of the rock. Thus, sample surfaces were polished gradually with finer sandpaper and using the oil-based diamond paste. Subsequently, the samples were grinded using 6 $\mu$ m diamond suspension, this process was followed by 3 $\mu$ m, 1 $\mu$ m, and in the last, quarter micron diamond suspension was used. Both locations sample surfaces were polished using the grinding and lapping machine by fixing the desired size of silicon carbide papers starting from 400 to 4000 mesh size.

## 3. Methodology

The illustration in Figure 4 provides the sequence of the micromechanical tests flow chart for analysis of Sembar shale samples. The details about experimental procedures are provided in subsequent sections of the manuscript.

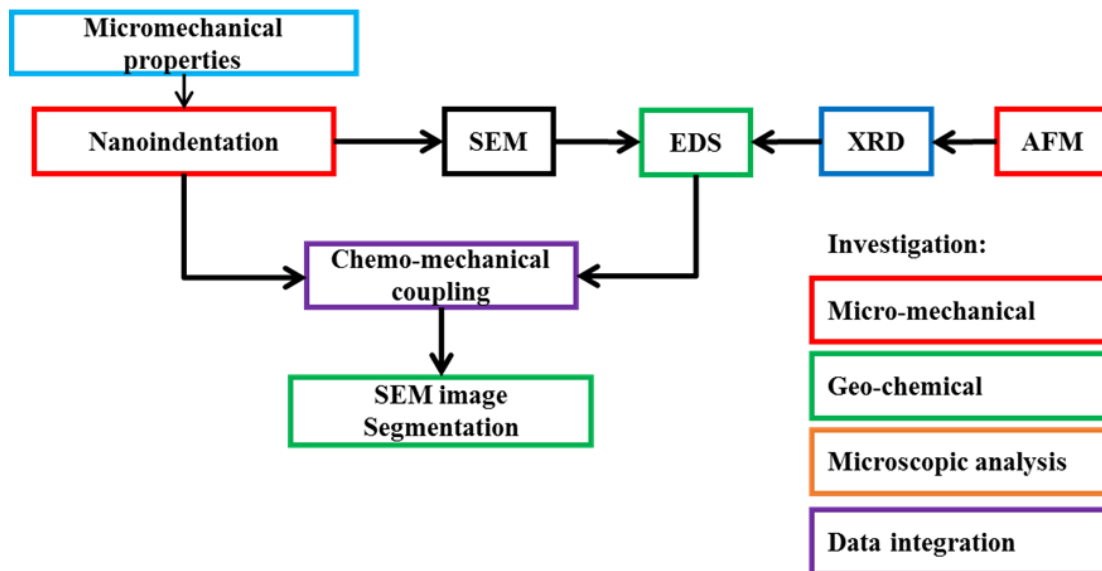


Fig. 4 Flowchart illustrates the coupled micromechanical and chemical analysis approach.

### 3.1 Atomic Force Microscopy (AFM)

For better visualizations of surface topography changes of Sembar shale formation, the experiments were performed using AFM model ezAFM+c10.20.16.51 Nanomagnetic imaging instrument with tapping mode. For the experimental details, the reader is referred to Bhutto et al. (2022) [8].

### 3.2 XRD Studies

For mineral compositional identification purposes, the samples were crushed, powdered, and tested via a diffractometer. Subsequently, the resulting fine powder of samples was analyzed, and data quantification was undertaken through mounting on an XRD instrument. The X'Pert Pro PANalytical diffractometer (model Malvern Panalytical, Malvern, UK) was used to identify the mineral phases. For details, readers are referred to our previous published papers [4, 41].

### 3.3 Scanning Electron Microscopy (Sem)

The surface features and micro-morphological characteristics of samples were assessed via SEM model JSM-6490L of JEOL Japan. The resin-impregnated samples of sizes ranging from 1 cm x 1cm were prepared. For the experimental procedural details, the readers are referred to Shar et al. 2022 [9].

### 3.4 Vickers' Micro Hardness Testing

Micro-indentation tests for the present study samples were carried out utilizing the Micro-Vickers Model 402 MVD hardness testing facility. The method of indentation testing mechanism employs load-controlled or depth-controlled techniques for the determination of the micro-mechanical properties. The Vickers hardness testing system is practiced by putting on the loads in the range between 0 and 300N with a resolution of 0.5 N. The loading rate also varies between 5–100 N/min. The apparatus can hold an indentation depth of around 2 mm with a precise resolution. Before testing hardness, the instrument should be calibrated for indentation depth, loads, and transducer.

### 3.5 Nanoindentation Principle

To assess the micromechanical behavior of Sembar shale, the nano-indentation tests were performed to obtain the rock hardness and elastic modulus. A typical nanoindentation moduli and its corresponding load-displacement curve be plotted after obtaining experimental data (as displayed in Figure 5a, b). By obtaining the load-displacement curve via Nanoindentation experiments, the load  $P$ , (mN) applied on any substance will be obtained via equation,

$$P = \alpha(h - h_f)^m \quad (1)$$

Where  $P$  is the load, mN,  $\alpha$ , and  $m$  are the fitting parameters,  $h$  is the displacement in nm and  $h_f$  is the indentation depth after achieving maximum load. The stiffness  $S$ , is obtained by using the following equation,

$$S = \frac{dP}{dh} h \quad (2)$$

The hardness ( $H$ ) of samples will be obtained through Nanoindentation moduli using the following equations,[42, 43]

$$H = \frac{F_{\max}}{A_p} \quad (3)$$

Where,  $F_{max}$  is the maximum load and  $A_p$  is the area under indentation.  $A_p$  is the contact area, which can be obtained via the following equation:

$$A_p = 24.5h_c^2 \quad (4)$$

The elastic modulus of shales was calculated using the following equation,

$$E = E^*(1 - \nu_s^2) \quad (5)$$

Further, the elastic moduli of the object would be obtained using the equation as described below,

$$E_r = \frac{\sqrt{\pi} \cdot S}{2 \cdot \beta \cdot \sqrt{A_p}(h_c)} \quad (6)$$

Where, in the above equation  $S$  is the material stiffness,  $A_p$  is the area under indentation,  $h_c$  is the indentation contact depth and  $\beta$  is the geometric constant and has values of 0.99. Moreover, the elastic strain moduli of shale samples would be determined using the following equation, [42, 44].

$$E^* = \frac{1}{\frac{1}{E_r} - \frac{1 - \nu_i^2}{E_i}} \quad (7)$$

Where  $E$  is the elastic modulus of the shale samples GPa, and  $\nu$  is the poisson's ratio  $E_i$ , is the indenter modulus elasticity, GPa;  $\mu$  is the Poisson's ratio,  $\mu_i$  is the Poisson's ratio,  $\gamma$  is the indenter modulus coefficient, and 1.034 is for Berkovich indenter.

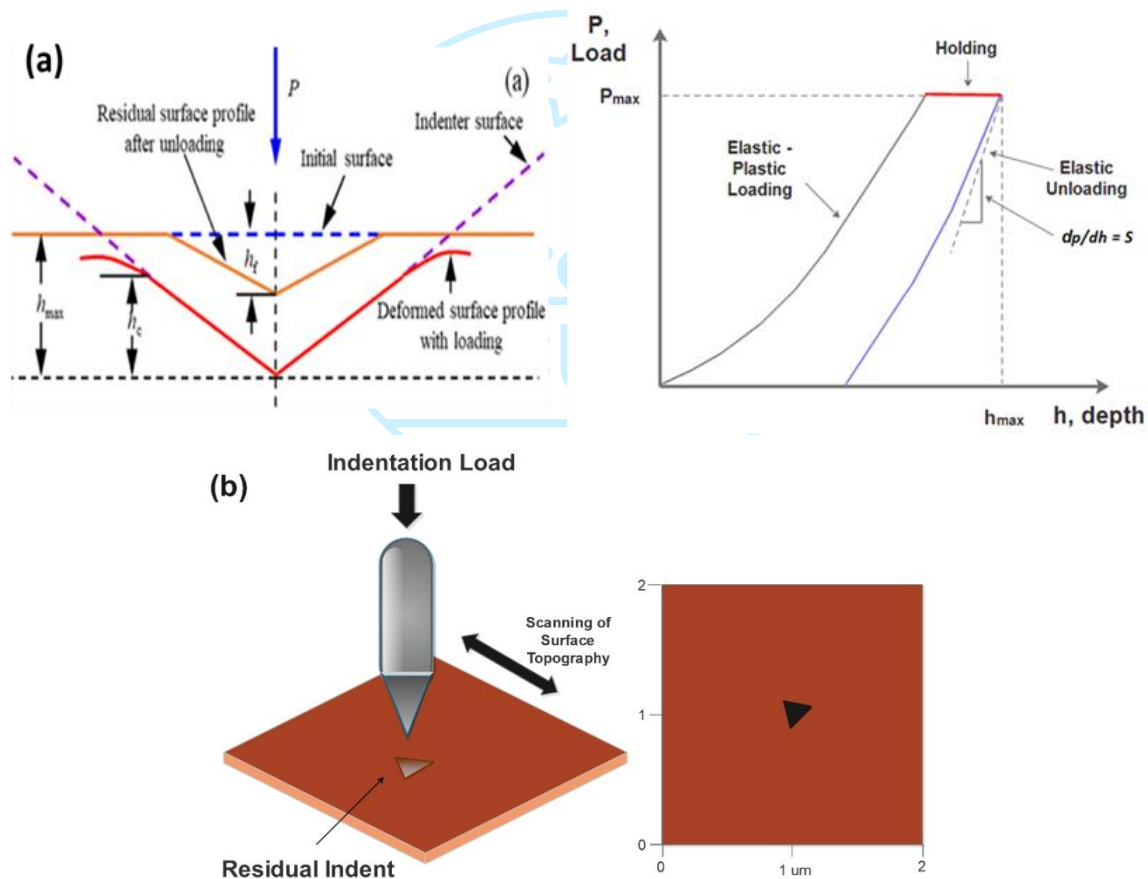


Fig. 5 The illustration shows the (a) Nanoindentation mechanics and typical load-displacement curve and (b) Schematic of nanoindenter to produce a topographical image via indentation tests (modified from Oliver and Pharr, 1992) [43].

### 3.6 Nanoindentation Experimental Procedure

Nanoindentation is extensively applied to determine the mechanical properties of materials such as hardness, elastic modulus, and fracture toughness at the nanoscale [45]. Usually, the nanoindentation tests are carried out on a high level of surface smoothness. The schematic of nanoindentation tests is shown in Figure 6. The indentation experiments were performed by considering four experimental stages (i) firstly, appropriate Indenter contact with the sample is established (ii) secondly, the desired load is established, where the load is applied to reach its maximum (iii) third stage is the holding stage in that the load is kept constant for few seconds and (iv) during fourth stage, the indenter applied load is released from the sample surface. Subsequently, the response of loading and unloading will be recorded. The tests were performed

with high accuracy so that the sample's permanent deformation must be avoided. It is recommended that the indentation point spacing should be at least  $50\mu\text{m}$ , hence this practice was followed in our experiments [19]. First, an indenter is used to apply the predetermined weight to the surface of a rock sample at a specific depth. After that, a brief period will be held constant to prevent any mistakes in the load method leading to the outcomes. After the load is released to the point of zero tension, the samples undergo elastic deformation. Subsequently, the gradual increase in load on the sample may result in plastic deformation. Finally, the load is to be released and the elastic deformation of the shale sample is restored. Eventually, the indenter penetrates the sample and automatically records the loads and corresponding indentation displacements. Further, the study set a maximum indentation force of  $50\text{mN}$ . Thereafter, the loads were held constant for 15 seconds at the peak load of  $50\text{mN}$ . The system produces hardness values based on built-in computational analytical methods [46].

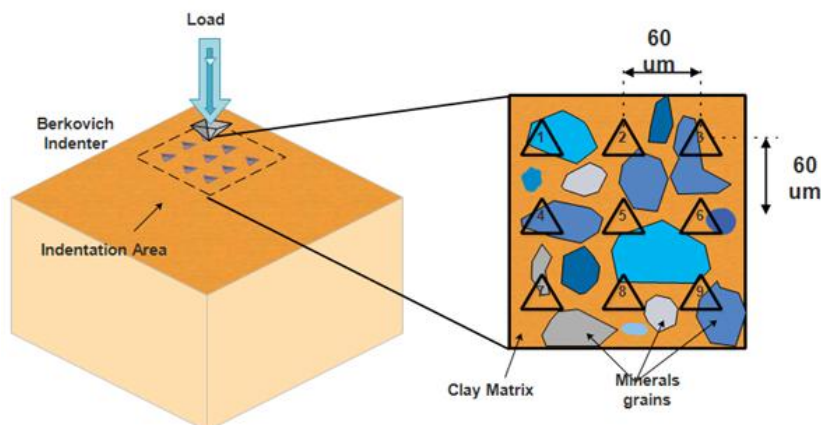


Fig. 6 Illustration is the diagram of nanoindentation test points (modified from Yiyu, et al. 2022) [34].

## 4. Results and Discussions

### 4.1 Surface Topography Via AFM

Atomic force microscopy (AFM) has been known to be a device that comprehensively examines the various material surfaces at nanoscale. To ensure that the sample surface was smooth for the micro- and nanoindentation tests, AFM experiments were conducted in this work. The AFM surface topography image captured is shown in Figure 7 (a, b), which reflects the sample's surface smoothness. In addition, this instrument can detect the changes in pore distribution and surface roughness of the samples. The surface roughness measurements obtained via AFM showed that it ranges from  $357\text{nm}$  to  $528\text{nm}$  for the shale samples studied.

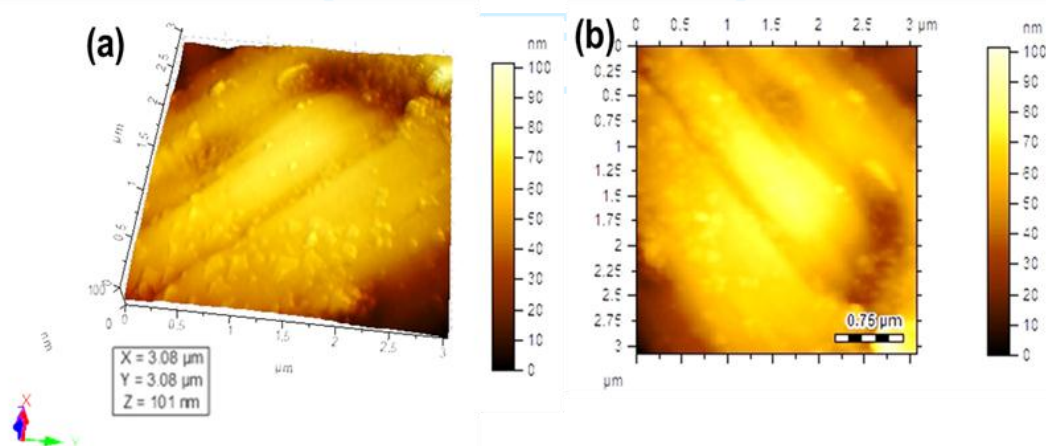
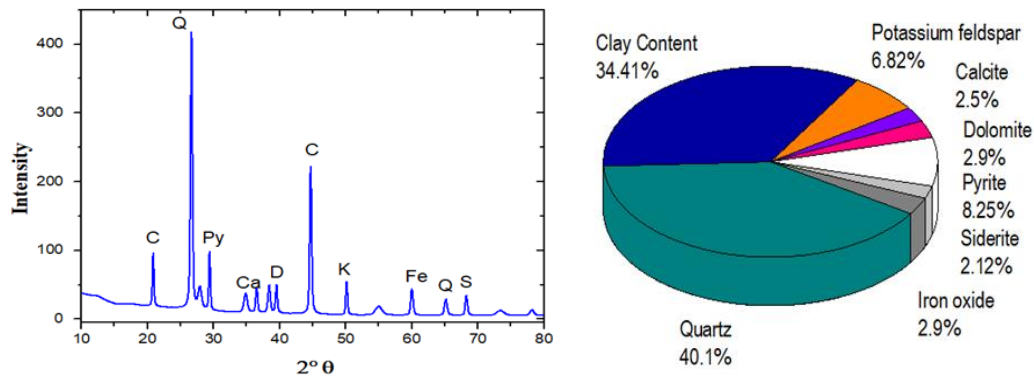


Fig. 7 Atomic Force Microscopy (AFM) images (a) 3D surface tomography (b) 2D height morphology

### 4.2 Mineralogical Composition and Characteristics via XRD

The XRD pattern along with different mineral proportions of the Sembar shale sample analysed is displayed in Figure 8. This shows that the predominant minerals were quartz and clay. The quartz was observed to be the first dominant mineral; its contents ranged from  $32.5\text{--}51.6\%$  with an average value of  $40.1\%$  and the second dominant mineral found was the clay contents which ranged from  $28.9\text{--}47.20\%$  with an average value of  $34.41\%$ . The rest of the minerals were in smaller quantities, such as, the potassium feldspars, pyrite, dolomite, calcite, siderite, and iron oxides with an average range were  $6.82\%$ ,  $8.25\%$ ,  $2.9\%$ ,  $2.5\%$ ,  $2.12\%$ , and  $2.9\%$ , respectively. In addition, this study performed EDX experiments to obtain the mineral composition. The EDX shows that the samples exhibit silicon and oxygen which reflects the quartz in the sample surfaces. Also, the presence of carbon in large quantities indicated that these shales possess organic matter. Although, the existence of other elements such as potassium, silicon, oxygen, and trace amounts of aluminium reveals the

presence of K-feldspars. Calcite's presence could be verified by the existence of calcium. Subsequently, the presence of iron and sulphur is the reflection of pyrite's existence.



**Fig. 8** Illustration represents the (a) XRD pattern and (b) shows the mineralogy of Sembar Shale.

Explanation: (Q-Quartz, C-Clay, K-potassium-feldspars, P-pyrite, D-dolomite, Ca-calcite, S-siderite, and Fe-iron oxides).

### 4.3 Micromechanical Properties of Shale

#### 4.3.1 Microhardness via Micro-Vickers

Micro-Vickers apply a precise indenter weight on the material at a fine scale change of impressed loads. Usually, it provides a sound basis for assessing the wellbore stability and rock strength parameters to design hydraulic fracturing of shale and tight reservoir formations. This has also implications in designing subsurface CO<sub>2</sub> sequestration operations [47]. Micro-indentation analysis was accomplished on samples from two different outcrop locations (i.e. A and B) to define the extent of rock mechanical strength. The Vickers' micro-hardness for shale samples A and B obtained is shown in Figure 9. The Vickers' micro-hardness for shale sample A ranges from 48.4 HV (Vickers' Hardness) to 63.6 HV with an average of 58.6 HV under the load of 980mN. However, for shale sample B hardness (HV) data ranges from 25.6 HV to 31.5 HV. The shale sample B hardness measured ranges from 18.7 HV to 25.40 with an average of 21.25 HV. It is obvious from our results that the hardness of the latter was lower than the former due to low compaction, and less dense grain packing of the samples. Overall, the micro-hardness tests results analysed showed that the sample A have larger values than the sample B. Generally, it is seen that the shale rocks are highly naturally cracked though their indentation toughness is affected by the surface roughness of the sample and indentation position [47]. The lower values of hardness from shale sample B imply that measurements made on samples may be underestimated, this raises uncertainty if the same is applied to in-situ conditions. Such data based on less compacted shale may also underestimate the cap-rock seal integrity during subsurface CO<sub>2</sub> storage.

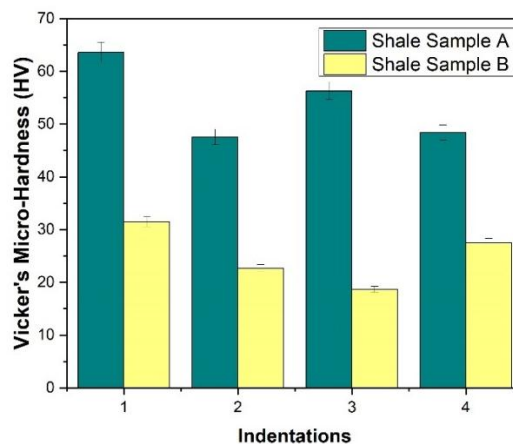


**Fig. 9** Average Vickers' micro-hardness of shale samples A and B.

#### 4.3.2 Load–Displacement Nanoindentation Curves

The elastic-plastic deformation i.e. load-displacement curves generated via indentation experiments for two samples are shown in Figure 10 and 11 corresponding to their indentation grid. It is obvious from load-displacement curves that most of the sample B responses are relatively close to each other. It appears that the sample B specifies relatively smaller deviations in their elasticity compared to shale sample A. Moreover, it is obvious from the sample B elastic-plastic deformation curve; the minerals grains of this sample are more homogenous and are fairly sorted. In contrast, the shale sample A load-displacement curves displayed substantial variations under the predesigned indentation loading conditions. The indentation depths of shale sample A are mostly deeper than 2000 nm, with the average indentation depths for sample B. Following the unloading process, the curves failed to revert to their initial position. This suggests that the sample experienced plastic deformation, accompanied by an increase in residual depth. The displacement curves under load offer valuable mechanical insights, enabling the calculation of the specimen's modulus and hardness. Additionally, they aid in

identifying non-linear events such as phase transformations, cracking, and delamination [48]. This implies that the micromechanical behavior of A shale considerably varies relating to its different indent points.

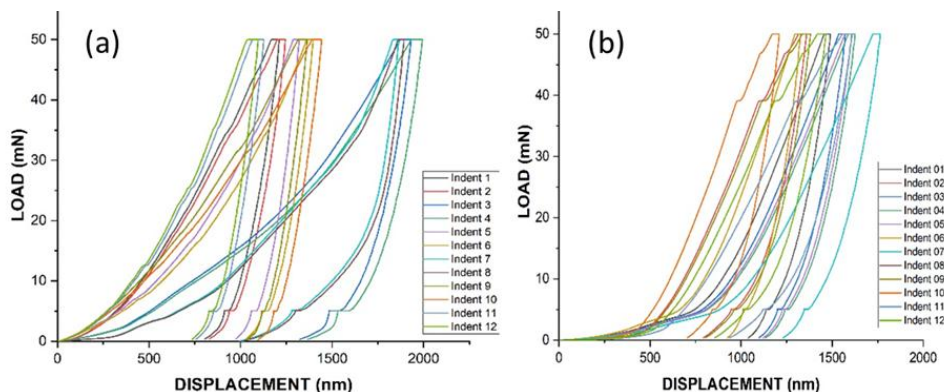


Fig. 10 Load-displacement curves (a) Shale sample A (b) shale sample B.

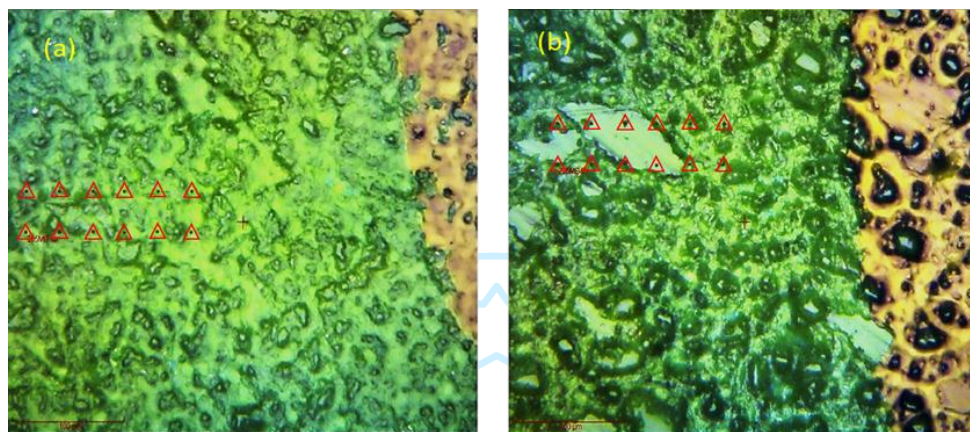


Fig. 11 Illustration shows the selected images of the nanoindentation grid on a map displaying the indent-marked locations for clarity. (a) shale sample A (b) shale sample B.

The shale reservoirs typically display diverse behavior because of the differences in the depositional environment, mineralogy, and microstructural features [49]. However, very few studies in the recent past have studied the impact of heterogeneity on shale formation mechanical behaviour [33, 34]. Shi et al. (2021) studied the effect of indent load holding times on shale micromechanical properties and they established that by changing indent load holding time to next higher level result into decreased hardness values[32]. The effect of heterogeneity previously was disregarded, since these investigations were conducted under the presumption that the materials are homogeneous. Nonetheless, the goal of the current study was to evaluate how variability affected the micromechanical characteristics of shale deposits.

The indentation forces describe that the larger the depths weaker the rock strength. B shale micromorphology shows that the sample has not developed micro-cracks, however, the micro-cracks were seen in A shale, because the cracks that appeared within these samples were due to stress relaxation, when samples were brought to surfaces. Additionally, due to rock brittle behaviors, the microcracks were also produced during indentation studies within shale sample A. The pop-in behavior, which is essentially a jump in the load-displacement curve, was seen within tested shale samples. Generally, the pop-in phenomenon appears in those samples which exhibit more brittle materials. Similar behaviors were also reported by other authors for example, in the shale rock formations from Longmaxi, micromechanical properties have also shown pop-in behaviors under nanoindentation experiments[33]. Such events are commonly noticed in the loading curves of porous samples from indentation experiments. The pop-in indicates an abrupt change in indenter displacements is noticed with an inconsequential rise in the curve under pre-set indentation loads. Though the pop-in behavior noticed within A shales might be attributed to the possible existence of grain boundary micro-crack network and fracture formed during indentation experiments [31, 33]. Other reasons for such abnormal behavior might be the void spaces, soft materials, and kerogen which have resulted into lower mechanical strength of shales [50-52]. The Present study observed smaller deviations in elastic deformation were noticed for all B samples load-displacement curves. On the other hand, the A shale samples showed relatively higher deviations in modulus of elasticity under indentation. the B samples were less compacted than A shales which exhibited dense structure, more brittle, and more compacted due to in-situ overburden stresses.

#### 4.4 Effect of Indentation Force on Micromechanical Properties of Sembar Shale

##### 4.4.1 Modulus of Elasticity and Histogram Results

The average elastic modulus via nano-indentation obtained for samples under constant loading conditions is displayed in Table 2 and Figure 12. These results include the Nano-indentation moduli (left) and corresponding histograms (right).

The hardness of the A Shale samples ranges from 9.08 GPa to 26.52 GPa with a mean of 20.34 GPa and the elastic moduli range from 15.63 to 29.34 GPa with a mean value of 22.57GPa. The hardness of B samples ranged from 6.73 to 24.24 GPa with an average value of 18.15 GPa and the elastic modulus ranged from 5.12 to 9.43 GPa with a mean value of 8.25 GPa. Thus, the results displayed that the B shales exhibited significantly lower hardness and modulus of elasticity than A shale samples. The lower indentation moduli usually display that the rock's mechanical characteristics are weaker/softer due to the lower compaction during sample preparation and other reasons could be the creation of fractures, micro-cracks, and clay swelling effects.

**Table 2** Average values of modulus of elasticity and hardness of intact shale and Synthetic shale.

Sample ID	Hardness (GPa)		Elastic Modulus (GPa)	
	Mean (GPa)	St. Deviations (GPa)	Mean (GPa)	St. Deviations (GPa)
Sample A	18.15	12.45	8.25	12.62
Sample B	20.34	10.62	22.57	10.78

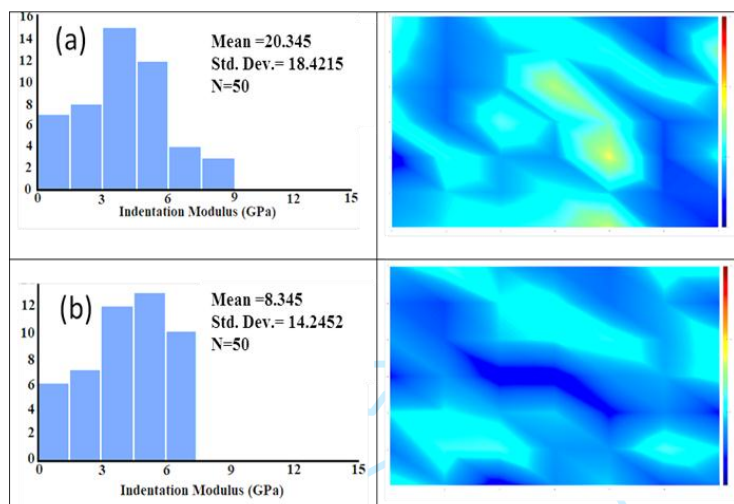


**Fig. 12** Illustration is the histogram (left) and Nanoindentation moduli (right), (a) shale sample A (b) shale sample B.

#### 4.4.2 Factors Affecting the Rock Hardness

Microstructural images of A and B shale samples are depicted in Figure 13. It is obvious that the A shale clay minerals are preferentially surrounded by fine-grained quartz and potassium feldspars which more likely occur in the clay matrix framework of rock as distinct grains. However, the B shale samples possess stiff quartz and feldspar grains and are larger, which in turn supports the clay framework of the sample matrix. In the B shale samples, it appears that the clay minerals are dispersed and fill the opening between intergranular void spaces of the particles. Generally, the depositional environment and subsequent diagenetic changes are responsible for the microstructure of shale formations. The existence of clay minerals plays a significant part in the establishment of diversified pore systems and porosities which ultimately affect the rock hardness and elasticity. Additionally, the microstructure observations showed different mineral types with dispersed intergranular arrangement, and the shapes and size of particles established cavities that were filled by calcite.

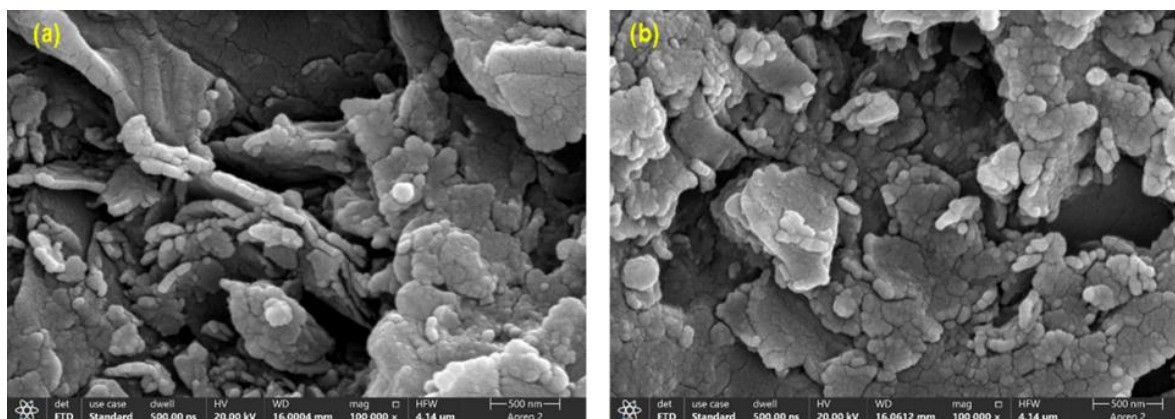


**Fig. 13 (a,b).** Scanning electron photomicrograph displays the micro-texture of samples from the Sembar shale formation.

For particle size distribution and difference in mineral orientation within the sample was examined by using Image J software. The differences in particle size of both samples i.e. A and B samples were determined via the watershed algorithm, which performs effective segmentation and particle size analysis of objects. Generally, different mineral grains display dissimilar brightness on SEM images with obvious boundaries. Thus, mineral particle orientation under the chosen region was identified using the watershed technique works well based on picture brightness levels[53, 54]. Thereafter, the statistical analysis was done on data acquisition of particle sizes. The algorithm involved in attributing the particle size data calculation, is coded and integrated via a plug-in termed MorphoLibJ and is associated with a visual

basic graphical interface (GUI). This is an effective technique for particle segmentation. Hence, the scanning electron photomicrograph and its selected area of  $520\ \mu\text{m} \times 450\ \mu\text{m}$  were taken into consideration to estimate the grain sizes. This was performed via binary images which exist within sample particles and share borders by touching each other boundaries. Subsequently, the segregation of different sizes of grains was performed. Thereafter, the different particles were acquired by deducting the binary image and a segmented binary image. The particle size proportions based on coarse and fine grains of a range of sizes occurring within the studied samples are depicted in Figure 14. Further, the sequence of particle segmentation and the relative amount of minerals corresponding to different equivalent radii is depicted in Figure 15. This shows that the A shale samples predominate the grain particles corresponding to their equivalent radii of  $<2\ \mu\text{m}$ . However, the B shale samples reveal that the large grain-size mineral particles are dominating. The mineral particles larger than  $>25\ \mu\text{m}$  were noticed within B shales.

It is generally perceived that hard minerals have analogous behaviors as coarse aggregates in construction industry concrete materials.[34] Similarly, the hard minerals were assembled within A shale samples in its clay matrix structure making a good bond among the mineral grains. In contrast, the B shale minerals were dispersed exhibiting weak bounding and embedment within the clay matrix due to lower compaction at the time of their preparation and it appears to be susceptible to plastic deformation. Moreover, if a hard mineral is found to be present in a dispersed form clay-bearing rock formation will not form a strong load-sustaining structure [34]. Subsequently, in this study as indenter load is applied and the indenter touches the clay-bearing matrix which poorly controls the indenter movement and shows plastic deformation. On the other hand, if load via nanoindentation is applied on tough minerals which may be detached from clay minerals leading to weak overall bonding of framework grains and may appear with small resistance towards indenter penetration, this phenomenon was observed within B shales with smaller hardness. On the other hand, if the indenter is lowered on the sample surface of hard mineral grain which is tightly packed as is the case of the A sample, the force applied experiences more resistance and the other framework grains are supported via closely arranged grain particles. Subsequently, the A shales will experience larger resistance to indenter penetration thus as a result greater large hardness was observed. Similar, findings are also reported by other authors in analysing shale samples mechanical properties [34].

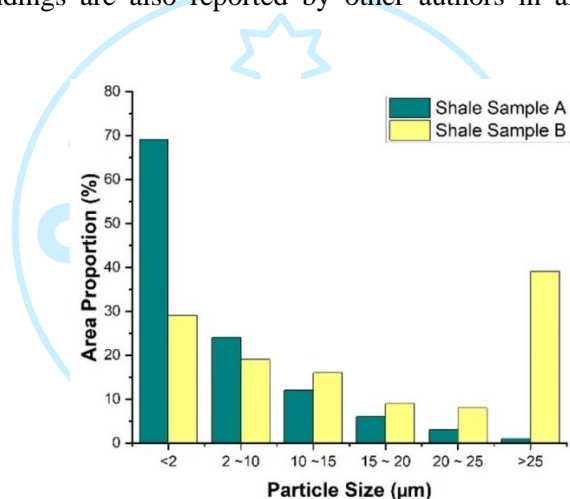


Fig. 14 Proportion of minerals with different particle sizes

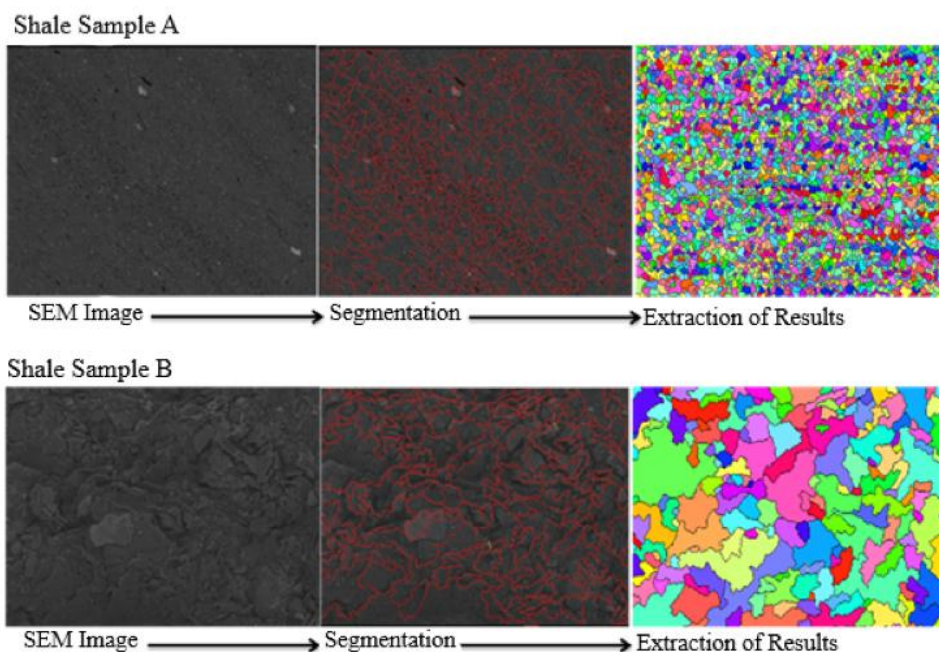
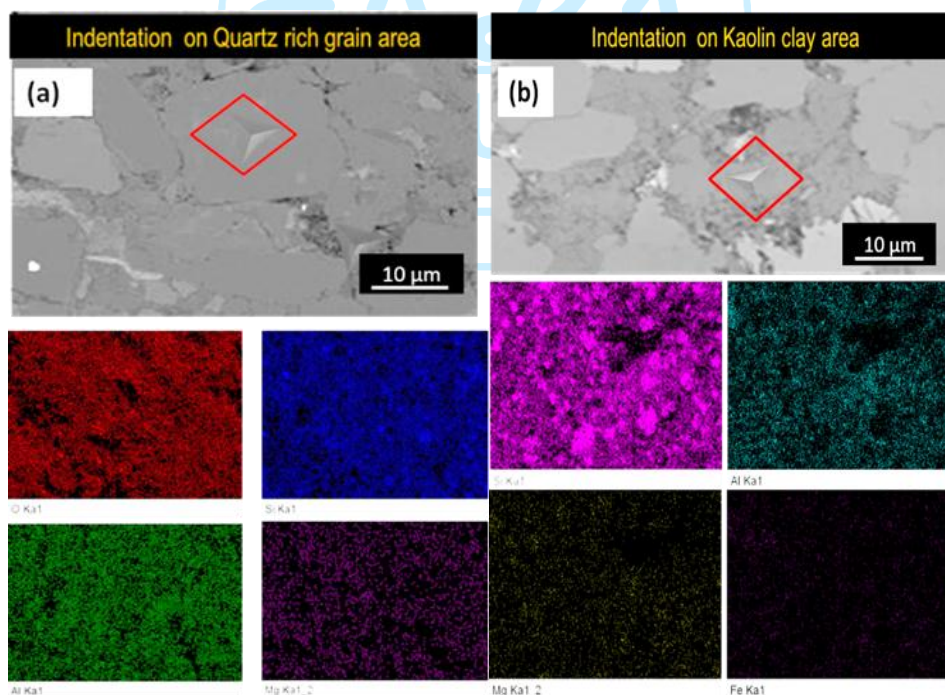


Fig. 15 Illustration shows the Shale mineral segmentation process via watershed image segmentation

#### 4.4.3 Analysis of the Modulus of Elasticity and Creep

Various factors influence the modulus of elasticity of shale samples including the pore morphology, microstructure and mineralogical composition. It is noteworthy, that different mineral grain particle's response to elastic modulus and hardness is different. Numerous studies have attempted to investigate the discrepancies in the elastic modulus and hardness of rock samples due to heterogeneous mineral grains [31, 33, 55]. Thus taking account of such differences, this paper has attempted to use the EDS image data to integrate with the micromechanical behavior of shales of the present study corresponding to their mineralogy. Thus, after indentation tests, the same samples were examined via EDS to obtain information about dispersed elements lying under the indentation test point as displayed in Figure 16. The purpose of such analysis was to connect the information derived from nanoindentation experiments related to the modulus of elasticity and hardness to the sample residual mineralogy. The information about local surface mineralogy was obtained via the generalized chemical formula of the rock-forming minerals. For instance, quartz is formed by rock surface areas dominated by silicon and oxygen elements. Subsequently, the various other minerals such as potassium-feldspars enriched areas were interpreted from potassium, silicon, aluminium, and oxygen elements presence[56]. Thus, the indentation of the A shale at points 2 and 3 from EDS analysis were recognized as quartz and clay minerals dominated areas respectively in Figure 16. The modulus of elasticity of these indentation points obtained was ranging from 30.42GPa, 26.38GPa, and 20.42GPa, respectively. The average elastic properties of complex shale formation are usually established based on its compound mineral constituents. For simplicity, a conceptual model developed explaining the impact of mineral arrangement on the modulus of elasticity and hardness is portrayed in Figure 16. A simplified model describing the influence of indenter load in two types of mineral grains (i) sand and (ii) clay (Figure 17). This illustrates that when an indenter load is applied to sand grains it shows slight compaction however, the load significantly affects the clay mineralogy. This shows that the main factor which are liable for differences in elastic properties of the sample is the heterogeneous distribution of mineral constituents. This is apprehended by our earlier interpretation related to mineralogy and microstructure effect on shale formations on micromechanical characteristics. Several other published studies have also reported similar findings which support the present study results [55]. For example, the micromechanical properties of clay-rich Longmaxi shale modulus elasticity behaved similarly to the present study results[34, 55, 57]. Thus for the shale formations the micromechanical properties i.e. modulus of elasticity are controlled by the mineralogy, samples microstructures, and pore morphologies. This has implications in drilling a well if the drill bit approaches hard formation during drilling and is not appropriately designed may lead to failure of the drill bit. Subsequently, the proppant embedment may also cause problems in many situations.



**Fig. 16** Illustrations display the SEM and EDS images corresponding to different indentation points. (a) The indentations at point 2 on load-displacement graph which is dominated by Si and O and is interpreted as quartz-rich (b) Indent point 3, in which Al, Si, Fe, and Mg occur more likely were recognized as clay dominated area.

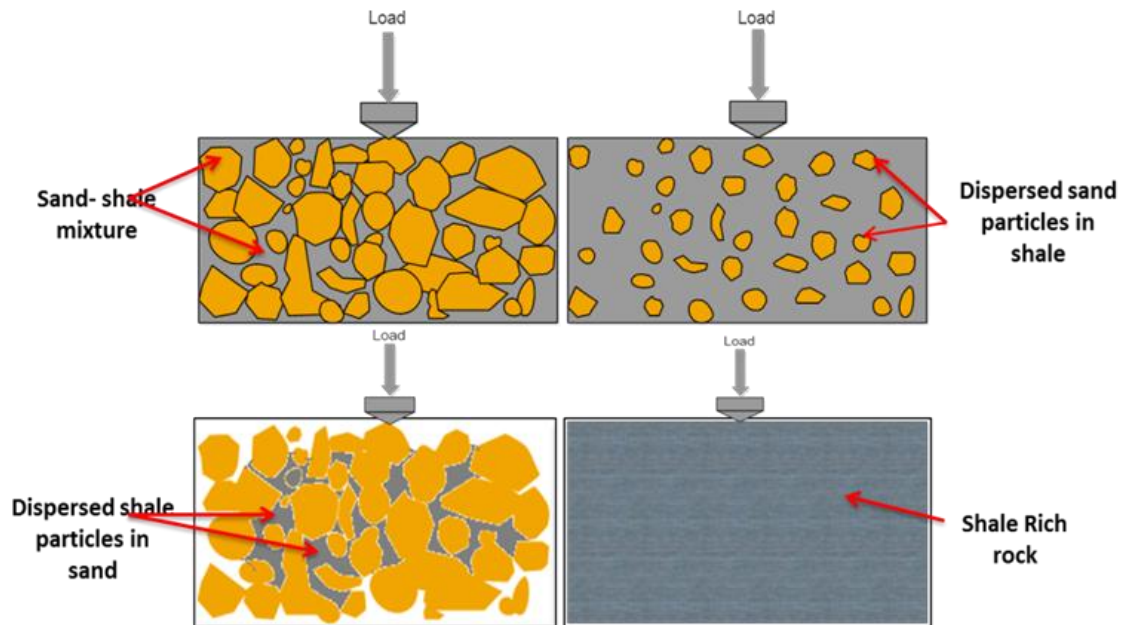


Fig. 17 A simplified conceptual model describes the effect of elasticity and hardness on grain particles within shale formation. (Figure is not drawn on scale)

## 5. Conclusions

The study conducted has reported results of a micromechanical characterization of the samples obtained from the Sembar shale formation in the Southern Indus Basin, Pakistan. This study performed load displacement nanoindentation tests which were integrated with SEM-EDS data analysis to attain the mechanical behaviour of the Sembar shale formation constituents. The results show a significant variation in both the hardness and elastic modulus of the A and B Sembar shales sample. The extent of variations in micromechanical characteristics is larger for earlier but later exhibited smaller changes in hardness and modulus of elasticity as observed from nanoindentation experiments. The variations noticed from elastic properties and hardness may be the result of changes in dispersed mineral grain sizes and their orientations. Subsequently, the grain packing and embedment in B shale samples displayed weak structure of framework grains which in turn have resulted in relatively lower hardness and elasticity. In contrast, the A shale samples resulted in higher values of hardness and elasticity due to the rigidity of the mineral of shale rock. Hence, the data extracted from B shales may underestimate the rock strength which in turn will propagate severe issues in predicting cap rock seal integrity. In addition, this may pose problems in drilling programs and proppant placement difficulties following fracturing treatments in shale reservoirs.

## Author Contributions

Darya Khan Bhutto: conceptualization, investigation, methodology, formal analysis, data curation, writing-original draft; Ubedullah Ansari: supervision, investigation, visualization, formal analysis, data curation, writing-review & editing; Aftab Ahmed Mahesar: supervision, investigation, visualization, formal analysis, data curation, writing-review & editing; Najeeb Anjum Soomro: methodology, formal Analysis, writing-review & editing.

## Conflicts of Interest

There are no conflicts to declare.

## Data Availability

The data that supports the findings of this study are not openly available till the finalization of the PhD study of the corresponding author. Afterwards, the complete data can be accessed via Higher Education Commission Pakistan website <https://www.hec.gov.pk/english/Pages/default.aspx> under which the PhD scholar university is registered and recognized.

## Acknowledgements

The authors are highly grateful to Dr. Muhammad Ali Edith Cowan University Australia for his assistance in nanoindentation experiments of Sembar shale samples. In addition, support from Dr. Fahd Nawaz Khan from GIK Institute of Engineering Sciences and Technology, Swabi, Pakistan for his assistance in nanoindentation experiments of Sembar shale samples are highly appreciated.

## References

1. A.A. Mahesar, A.M. Shar, M. Ali, A.H. Tunio, M.A. Uqailli, U.S. Mohanty, H. Akhondzadeh, S. Iglauer, A. Keshavarz, Morphological and petro physical estimation of eocene tight carbonate formation cracking by cryogenic liquid nitrogen; a case study of Lower Indus basin, Pakistan, *Journal of Petroleum Science and Engineering*, 192 (2020) 107318.
2. M. Ali, B. Pan, N. Yekeen, S. Al-Anssari, A. Al-Anazi, A. Keshavarz, S. Iglauer, H. Hoteit, Assessment of wettability and rock-fluid interfacial tension of caprock: Implications for hydrogen and carbon dioxide geostorage, *International Journal of Hydrogen Energy*, 47 (2022) 14104-14120.
3. A.M. Shar, A.A. Mahesar, K.R. Memon, Could shale gas meet energy deficit: its current status and future prospects, *Journal of petroleum exploration and production technology*, 8 (2018) 957-967.
4. A.A. Mahesar, M. Ali, A.M. Shar, K.R. Memon, U.S. Mohanty, H. Akhondzadeh, A.H. Tunio, S. Iglauer, A. Keshavarz, Effect of cryogenic liquid nitrogen on the morphological and petrophysical characteristics of tight gas sandstone rocks from kirthar fold belt, Indus Basin, Pakistan, *Energy & Fuels*, 34 (2020) 14548-14559.
5. M. Ali, A.M. Shar, N. Yekeen, H. Abid, M.S. Kamal, H. Hoteit, Impact of methylene blue on enhancing the hydrocarbon potential of early cambrian Khewra sandstone formation from the Potwar Basin, Pakistan, *ACS omega*, 8 (2023) 47057-47066.
6. W.A. Abro, A.M. Shar, K.S. Lee, A.A. Narejo, An integrated analysis of mineralogical and microstructural characteristics and petrophysical properties of carbonate rocks in the lower Indus Basin, Pakistan, *Open Geosciences*, 11 (2019) 1151-1167.
7. A.M. Shar, A.A. Mahesar, G.R. Abbasi, A.A. Narejo, A.A.A.D. Hakro, Influence of diagenetic features on petrophysical properties of fine-grained rocks of Oligocene strata in the Lower Indus Basin, Pakistan, *Open Geosciences*, 13 (2021) 517-531.
8. D.K. Bhutto, A.M. Shar, G.R. Abbasi, U. Ansari, Shale Wettability Characteristics via Air/Brines and Air/Oil Contact Angles and Influence of Controlling Factors: A Case Study of Lower Indus Basin, Pakistan, *ACS Omega*, (2022).
9. A.M. Shar, M. Ali, D.K. Bhutto, A. Alanazi, H. Akhondzadeh, A. Keshavarz, S. Iglauer, H. Hoteit, Cryogenic Liquid Nitrogen Fracking Effects on Petro-Physical and Morphological Characteristics of the Sembar Shale Gas Formation in the Lower Indus Basin, Pakistan, *Energy & Fuels*, (2022).
10. D.N. Dewhurst, J. Sarout, C. Delle Piane, A.F. Siggins, M.D. Raven, Empirical strength prediction for preserved shales, *Marine and Petroleum Geology*, 67 (2015) 512-525.
11. N. Sheikh, P.H. Giao, Evaluation of shale gas potential in the lower cretaceous Sembar formation, the southern Indus basin, Pakistan, *Journal of natural gas science and engineering*, 44 (2017) 162-176.
12. B. Ahmed, M. Mohibullah, S. Jalal, S.A. Abbasi, A.S. Khan, H. Rehman, Evaluation of Gas Potential in Early Cretaceous Shale Lower Indus Basin, Pakistan, *International Journal of Economic and Environmental Geology*, 11 (2020) 123-129.
13. M. Hosseini, M. Ali, J. Fahimpour, A. Keshavarz, S. Iglauer, Calcite-Fluid Interfacial Tension: H<sub>2</sub> and CO<sub>2</sub> Geological Storage in Carbonates, *Energy & Fuels*, 37 (2023) 5986-5994.
14. F. Alhamad, R. Sedev, M. Ali, M. Ali, H. Hoteit, S. Iglauer, A. Keshavarz, Effect of methyl orange on the hydrogen wettability of sandstone formation for enhancing the potential of underground hydrogen storage, *Energy & Fuels*, 37 (2023) 6149-6157.
15. Z. Jin-Chuan, Y. Chao, C. Jian, D. Qian-Ru, Deposition and distribution of potential shales in China, *Earth Science Frontiers*, 23 (2016) 74.
16. J.D. Arthur, B. Bohm, M. Layne, Hydraulic fracturing considerations for natural gas wells of the Marcellus Shale, (2009).
17. S. Heng, Y. Guo, C. Yang, J.J. Daemen, Z. Li, Experimental and theoretical study of the anisotropic properties of shale, *International Journal of Rock Mechanics and Mining Sciences*, 74 (2015) 58-68.
18. S. Heng, X. Li, X. Liu, Y. Chen, Experimental study on the mechanical properties of bedding planes in shale, *Journal of Natural Gas Science and Engineering*, 76 (2020) 103161.
19. P. Jia, S. Nadimi, J. Jia, Quantitative micro mechanical and pore structural characterisation of coal before and after freezing, *Fuel*, 316 (2022) 123421.
20. X. Shi, Z. He, S. Long, Y. Peng, D. Li, S. Jiang, Loading rate effect on the mechanical behavior of brittle longmaxi shale in nanoindentation, *International Journal of Hydrogen Energy*, 44 (2019) 6481-6490.
21. S. Xian, S. Jiang, L. Shuangfang, H. Zhiliang, L. Dongjie, W. Zhixuan, X. Dianshi, Investigation of mechanical properties of bedded shale by nanoindentation tests: A case study on Lower Silurian Longmaxi Formation of Youyang area in southeast Chongqing, China, *Petroleum Exploration and Development*, 46 (2019) 163-172.
22. S. Graham, M. Rouainia, A. Aplin, P. Cubillas, T. Fender, P. Armitage, Geomechanical characterisation of organic-rich calcareous shale using AFM and nanoindentation, *Rock mechanics and rock engineering*, 54 (2021) 303-320.
23. Q. Lyu, X. Long, P. Ranjith, J. Tan, Y. Kang, Experimental investigation on the mechanical behaviours of a low-clay shale under water-based fluids, *Engineering Geology*, 233 (2018) 124-138.

24. H. Sone, M.D. Zoback, Mechanical properties of shale-gas reservoir rocks—Part 2: Ductile creep, brittle strength, and their relation to the elastic modulus, *Geophysics*, 78 (2013) D393-D402.
25. J.W. Carey, M. Torsæter, Shale and Wellbore Integrity, *Shale: Subsurface Science and Engineering*, (2019) 145-159.
26. X. Fang, H. Feng, F. Li, H. Wang, Experimental investigation of the mechanical properties of mud shale under water-bearing conditions and its applications, *Scientific Reports*, 12 (2022) 1-11.
27. S.M. Lalji, M.A. Khan, J. Haneef, S.I. Ali, A.H. Arain, S.S. Shah, Nano-particles adapted drilling fluids for the swelling inhibition for the Northern region clay formation of Pakistan, *Applied Nanoscience*, (2021) 1-15.
28. C. Cai, F. Gao, G. Li, Z. Huang, P. Hou, Evaluation of coal damage and cracking characteristics due to liquid nitrogen cooling on the basis of the energy evolution laws, *Journal of Natural Gas Science and Engineering*, 29 (2016) 30-36.
29. C. Cai, Z. Tao, K. Ren, S. Liu, Y. Yang, Y. Feng, S. Su, P. Hou, Experimental investigation on the breakdown behaviours of sandstone due to liquid nitrogen fracturing, *Journal of Petroleum Science and Engineering*, 200 (2021) 108386.
30. W. Chen, M. Li, T. Zhang, Y.-T. Cheng, C.-M. Cheng, Influence of indenter tip roundness on hardness behavior in nanoindentation, *Materials Science and Engineering: A*, 445 (2007) 323-327.
31. G. Dong, P. Chen, A comparative experiment investigate of strength parameters for Longmaxi shale at the macro- and mesoscales, *International Journal of Hydrogen Energy*, 42 (2017) 20082-20091.
32. X. Shi, S. Jiang, L. Yang, M. Tang, D. Xiao, Modeling the viscoelasticity of shale by nanoindentation creep tests, *International Journal of Rock Mechanics and Mining Sciences*, 127 (2020) 104210.
33. Y. Long, Y. Zhang, X. Huang, Y. Wang, Y. Zhao, R. Wang, F. Song, Assessment of the Multiphase Mechanical Properties of the Longmaxi Formation Shale Using Nanoindentation Tests, *ACS omega*, 6 (2021) 18200-18214.
34. Y. Lu, Q. Cheng, J. Tang, W. Liu, H. Li, J. Liu, Z. Xu, R. Tian, X. Sun, Differences in micromechanical properties of shales from different depositional environment: A case study of Longmaxi marine shale and Yanchang continental shale using nanoindentation, *Journal of Natural Gas Science and Engineering*, (2022) 104727.
35. A. Fatmi, I. Hyderi, M. ANWAR, J. Mengal, Stratigraphy of Zidi formation (Ferozabad group) and Parh group (Mona Jhal group) Khuzdar district, Baluchistan, Pakistan, (1986).
36. V.-u.-N. Quadri, S. Shuaib, Hydrocarbon prospects of southern Indus basin, Pakistan, *AAPG bulletin*, 70 (1986) 730-747.
37. I. Kadri, *Petroleum Geology of Pakistan: Pakistan Petroleum Limited Karachi*, Pakistan, 1995.
38. A. Fatmi, Mesozoic, Stratigraphy of Pakistan, 12 (1977) 29-56.
39. M.D. Williams, 19. Stratigraphy of the Lower Indus Basin, West Pakistan, 5th World petroleum congress, OnePetro, 1959.
40. G.M. Sohail, C.D. Hawkes, Q. Yasin, An integrated petrophysical and geomechanical characterization of Sembar Shale in the Lower Indus Basin, Pakistan, using well logs and seismic data, *Journal of Natural Gas Science and Engineering*, 78 (2020) 103327.
41. A.M. Shar, M.F. Qureshi, D.k. Bhutto, F.H. Memon, Wettability Alteration of Limestone Carbonate Cores Using Methylene Blue and Alumina-Based Nanofluid: Implications for EOR, *Applied Sciences*, 13 (2023) 8474.
42. M. Doerner, D. Gardner, W. Nix, Plastic properties of thin films on substrates as measured by submicron indentation hardness and substrate curvature techniques, *Journal of Materials Research*, 1 (1986) 845-851.
43. W.C. Oliver, G.M. Pharr, An improved technique for determining hardness and elastic modulus using load and displacement sensing indentation experiments, *Journal of materials research*, 7 (1992) 1564-1583.
44. G. Pharr, W. Oliver, Measurement of thin film mechanical properties using nanoindentation, *Mrs Bulletin*, 17 (1992) 28-33.
45. F.M. Borodich, The Hertz-type and adhesive contact problems for depth-sensing indentation, *Advances in Applied Mechanics*, 47 (2014) 225-366.
46. W.C. Oliver, G.M. Pharr, Measurement of hardness and elastic modulus by instrumented indentation: Advances in understanding and refinements to methodology, *Journal of materials research*, 19 (2004) 3-20.
47. Q. Han, P. Chen, T. Ma, Influencing factor analysis of shale micro-indentation measurement, *Journal of Natural Gas Science and Engineering*, 27 (2015) 641-650.
48. F.-J. Ulm, Y. Abousleiman, The nanogranular nature of shale, *Acta Geotechnica*, 1 (2006) 77-88.
49. J. Wang, C. Yang, Y. Liu, Y. Li, Y. Xiong, Using nanoindentation to characterize the mechanical and creep properties of shale: load and loading strain rate effects, *ACS omega*, 7 (2022) 14317-14331.
50. D. Ma, C.W. Ong, T. Zhang, An improved energy method for determining Young's modulus by instrumented indentation using a Berkovich tip, *Journal of Materials Research*, 23 (2008) 2106-2115.
51. H.G. Chuah, Z.M. Ripin, Quantifying the surface roughness effect in microindentation using a proportional specimen resistance model, *Journal of Materials Science*, 48 (2013) 6293-6306.
52. K. Liu, M. Ostadhassan, B. Bubach, Applications of nano-indentation methods to estimate nanoscale mechanical properties of shale reservoir rocks, *Journal of Natural Gas Science and Engineering*, 35 (2016) 1310-1319.

53. P. Sarkar, A. Kumar, K.H. Singh, R. Ghosh, T.N. Singh, Pore system, microstructure and porosity characterization of Gondwana shale of Eastern India using laboratory experiment and watershed image segmentation algorithm, *Marine and Petroleum Geology*, 94 (2018) 246-260.
54. D. Chandra, V. Vishal, A critical review on pore to continuum scale imaging techniques for enhanced shale gas recovery, *Earth-Science Reviews*, 217 (2021) 103638.
55. J. Du, A.J. Whittle, L. Hu, T. Divoux, J.N. Meegoda, Characterization of meso-scale mechanical properties of Longmaxi shale using grid microindentation experiments, *Journal of Rock Mechanics and Geotechnical Engineering*, 13 (2021) 555-567.
56. X. Shi, S. Jiang, Z. Wang, B. Bai, D. Xiao, M. Tang, Application of nanoindentation technology for characterizing the mechanical properties of shale before and after supercritical CO<sub>2</sub> fluid treatment, *Journal of CO<sub>2</sub> Utilization*, 37 (2020) 158-172.
57. Y. Liu, S. Liu, Y. Kang, Probing nanomechanical properties of a shale with nanoindentation: heterogeneity and the effect of water–shale interactions, *Energy & Fuels*, 35 (2021) 11930-11946.

